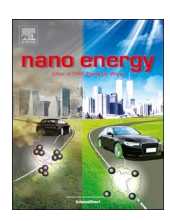


Contents lists available at ScienceDirect

Nano Energy

journal homepage: www.elsevier.com/locate/nanoen



Full paper

B₄C nanoskeleton enabled, flexible lithium-sulfur batteries

Ningning Song, Zan Gao, Yunya Zhang, Xiaodong Li*

Department of Mechanical and Aerospace Engineering, University of Virginia, 122 Engineer's Way, Charlottesville, VA 22904-4746, USA



ARTICLE INFO

Keywords:
Boron carbide
Nanowires
Lithium sulfur battery
Reduced graphene oxide
Hierarchical structure

ABSTRACT

Wise selection of host materials and judicious design of electrodes are critical for constructing high-performance energy storage devices. Here we report an unusual cathode configuration for lithium-sulfur (Li-S) batteries employing B_4C nanowires (BC-NWs) as a skeleton, porous activated cotton textile (ACT) as a flexible carbon scaffold, and reduced graphene oxide (rGO) as a self-adaptive protective shell. This BC-NWs@ACT/S/rGO cathode achieved superlative sulfur confinement and electrochemical performance with excellent cycling stability (over 1000 cycles at a high current density of $1.5 \, \text{mA/cm}^2$), an ultralow capacity decay rate (0.056% per cycle) and remarkable capacities at a wide range of discharging rate from $0.1 \, \text{to} \, 1.5 \, \text{mA/cm}^2$, demonstrating its potential to achieve high capacity and long cycle life simultaneously in Li-S batteries.

1. Introduction

Developing advanced energy-storage systems becomes paramount due to the continuously increasing demand of energy consumptions and rising concerns about environmental issues [1-4]. Owing to the stern reality that conventional lithium-ion batteries (LIBs) are approaching their theoretical limit [5-9], lithium-sulfur (Li-S) battery is considered as one of the most promising energy storage devices for electric vehicles, portable electronics, and even grid-scale storage devices [10]. Li-S chemistry offers superior theoretical specific capacity (1673 mAh/g) while natural abundance sulfur endows low cost and environmental compatibility [11]. Coupling with lithium metal, the assembled Li-S battery has a specific energy of 2600 W h/kg, which is more than five times higher than that of state-of-the-art lithium-ion batteries [12]. Despite the obvious advantages of Li-S batteries, many challenges need to be addressed before practical implementation, by and large, due to severe capacity decay, poor cycle life, low utilization of sulfur, and bad coulombic efficiency [13]. This dilemma can be primarily ascribed to the low electrical conductivities of sulfur, dissolution of intermediate polysulfides ($\text{Li}_x S_n$, $3 \le n \le 8$), and structural collapse induced by large volume variation (~80%) during solid-solid conversion between sulfur and Li₂S [14,15].

Aforementioned issues have sparked considerable interests in the configuration and rational design of Li-S battery cathodes to increase the sulfur utilization, immobilize polysulfides, and enhance battery's structural stability. Advanced carbon materials, such as porous carbon, carbon nanotube and graphene [16,17], have been extensively studied and widely utilized in various devices, such as supercapacitors [18],

solar cells [19,20], piezoresistive sensors [21], and strain sensors [22]. To date, the most common cathode design is to impregnate sulfur into various carbon matrices, such as amorphous carbon [23], carbon nanotube [24], and graphene [25–27]. Although substantial progress has been made, carbon-based materials alone are insufficient for high-performance Li-S batteries, especially the ones assembled in the flexible/wearable electronic devices, because it is still very challengeable to simultaneously increase the sulfur content, inhibit the "shuttle effect", and ensure mechanical stability of the electrode [28–30].

To address these issues, many efforts and improvements have been made to encapsulate sulfur with novel materials to mitigate capacity decay and enhance cycling performance, especially by employing carbides due to their chemical and mechanical stabilities [31,32]. Boron carbide (B₄C), one of the third hardest materials known in nature [33], is distinguished from other materials by its eminent physical and mechanical properties such as low density (2.5 g/cm³), high melting point (exceeding 2400 °C), extreme hardness (27.4–37.7 GPa), high elastic modulus (460 GPa), outstanding corrosion resistance, and high thermal stability [34]. In addition, at the nanometer scale, B₄C nanowires are ductile, without cracking when being bent to an included angle of 70 ° [35]. Such exceptional properties make B₄C a promising electrode material for batteries and fuel cells [36–41]. However, to the best of our knowledge, the investigation on B₄C as the electrode material for Li-S batteries is rare, let alone its further design and production.

Here, we report a rational design and implementation of a flexible, free-standing cathode for Li-S batteries with B₄C nanowires (BC-NWs) as the skeleton. In specific, porous activated cotton textile (ACT) was applied as the framework, and BC-NWs@ACT composite was obtained

E-mail address: xl3p@virginia.edu (X. Li).

^{*} Corresponding author.

by in-situ synthesizing the self-assembled high-density BC-NWs on the ACT via a conventional vapor-liquid-solid (VLS) [42] process. Then the preparation of a binder-free cathode for Li-S batteries was realized by impregnating elemental melted sulfur into the as-synthesized BC-NWs@ACT composite to form BC-NWs@ACT/S, and in further wrapping the BC-NWs@ACT/S with reduced graphene oxide (rGO) sheets that serve as the self-adaptive protective shell. This novel hierarchically configured cathode (BC-NWs@ACT/S/rGO) successfully confined sulfur in the three-dimensional interconnected framework while being flexible and mechanically robust. Ultimately, the Li-S cell with BC-NWs@ACT/ S/rGO as the cathode exhibited excellent cycling stability (over 1000 cycles), an ultralow capacity decay rate (0.056% per cycle) and high capacities at a range of discharging rate from 0.1 to 1.5 mA/cm². The flexible free-standing BC-NWs@ACT/S/rGO cathode was also assembled into a lightweight and foldable Li-S battery, which retained a high specific capacity and excellent mechanical stability, confirming its practical usage as a flexible power source.

2. Experimental Section

2.1. Preparation of BC-NWs@ACT/S/rGO hybrid cathode

As depicted in Fig. 1, BC-NWs@ACT hybrid structure was directly synthesized according to our previously established method [43,44]. A Ni-B emulsion was mixed by dissolving 7 g of Ni(NO₃)₂·6H₂O and 4 g of amorphous boron powders into 10 ml of ethanol under ultrasonic vibration. A piece of cotton textile was immersed in the Ni-B emulsion and dried at 70 °C in a preheated oven for 3 h. The BC-NWs@ACT hybrid structure was synthesized in a horizontal alumina tube furnace (diameter: 60 mm, length: 790 mm). The nickel- and boron-loaded cotton textile was placed in the middle of the tube furnace and heated to 1160 °C for 2 h with 300 sccm (standard cubic centimeter) continuous flow of argon at atmospheric pressure. BC- NWs@ACT/S nanocomposite was prepared via a melt-diffusion method. Sulfur powders were loaded onto the as-synthesized BC-NWs@ACT plate and heated to 156 °C for 10 h in a sealed autoclave.

In a typical procedure, graphene oxide (GO) solution with a concentration of ~4 mg/ml was produced using modified hummers method [45] from pure graphite powders. A piece of BC-NWs@ACT/S nanocomposite was dipped in the GO solution and dried for 6 h at 70 °C. The obtained hybrid structure was further thermally treated at 200 °C for 2 h in a sealed autoclave to vaporize any superfluous sulfur and partially reduce the GO to conductive rGO. BC-NWs@ACT/rGO hybrid structure with the same size was produced following the above-mentioned process as a reference to calculate the loading of sulfur. The

sulfur loading of the BC-NWs@ACT/S/rGO hybrid cathode was measured to be $\sim 3.0 \, \text{mg/cm}^2$. As shown in Fig. S1, the mass ratio of active S was calculated to be 77.6 wt% using thermogravimetric analysis (TGA; Q50, TA Instruments).

A piece of ACT was synthesized by directly heating the blank cotton textile to $1160\,^{\circ}\text{C}$ with 300 sccm continuous flow of argon in the tube furnace. Sulfur powders were respectively loaded onto the ACT and the BC-NWs@ACT plates without rGO coating, and heated to $156\,^{\circ}\text{C}$ for $10\,\text{h}$ and $200\,^{\circ}\text{C}$ for $2\,\text{h}$. The as-synthesized ACT/S and BC-NWs@ACT/S hybrid cathodes served as control samples and the mass of loading sulfur was controlled to be $\sim 3.0\,\text{mg/cm}^2$.

2.2. Materials characterization

The morphology and compositions of the as-synthesized samples were characterized and analyzed by scanning electron microscopy (SEM, Quanta 650), high-resolution transmission electron microscopy (HRTEM, FEI Titan 80), energy dispersive X-ray spectroscopy (EDX on the SEM and HRTEM), X-ray diffraction (XRD, PANalytical X'Pert Pro MPD), X-ray photoelectron spectroscopy (XPS, ULVAC-PHI, Inc.), and Raman spectroscopy (Raman, Renishaw InVia Raman microscope at 514 nm). The specific surface area of the composite was measured using a Quantachrom Autososrb iQ nitrogen adsorption—desorption analyzer and measured with the Brunauer–Emmet–Teller (BET) theory.

2.3. Battery assembly and electrochemical testing

To characterize the electrochemical properties of the as-synthesized cathode, CR2032 type coin cells were assembled by using MTI MSK-110 crimping machine in an argon-filled glove box (Mbraun, Germany), with BC-NWs@ACT/S/rGO as a cathode, lithium metal as an anode and Celgard 2400 film as a separator, respectively. Specific capacity values and charge/discharge rates were calculated based on the mass of active materials (sulfur). The electrolyte solution was prepared by dissolving 1 M lithium bis(trifluoromethanesulfonyl)imid (LiTFSI) and 0.2 M LiNO₃ in 1,3-dioxolane (DIOX)/1,2- dimethoxyethane (DME) (1:1, by volume). For comparison, the ACT/S, ACT/S/rGO, and BC-NWs@ACT/ S cathodes were also assembled into CR2032 type coin cells as the control samples. To demonstrate the excellent mechanical properties and flexibility of BC-NWs@ACT/S/rGO, the flexible Li-S cell was assembled using the binder-free BC-NWs@ACT/S/rGO nanocomposite directly as the cathode. Galvanostatic charge/discharge measurements were performed at different rates in the voltage range of 1.3-3 V versus Li/Li⁺ using a LAND CT2003A battery tester. A CHI 660E electrochemical workstation was used to measure the cyclic voltammograms

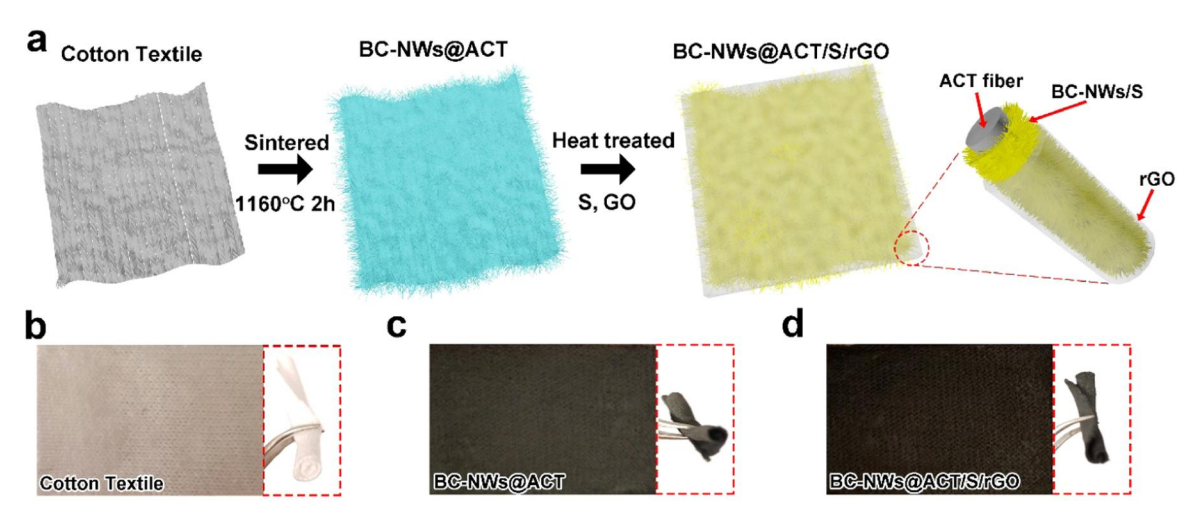


Fig. 1. (a) Schematic illustration of the design principle and synthesis process of BC-NWs@ACT/S/rGO hybrid structure. (b,c,d) Digital images of cotton textile, BC-NWs@ACT and BC-NWs@ACT/S/rGO samples. The corresponding samples under folded state are also imaged, as shown in the inset.

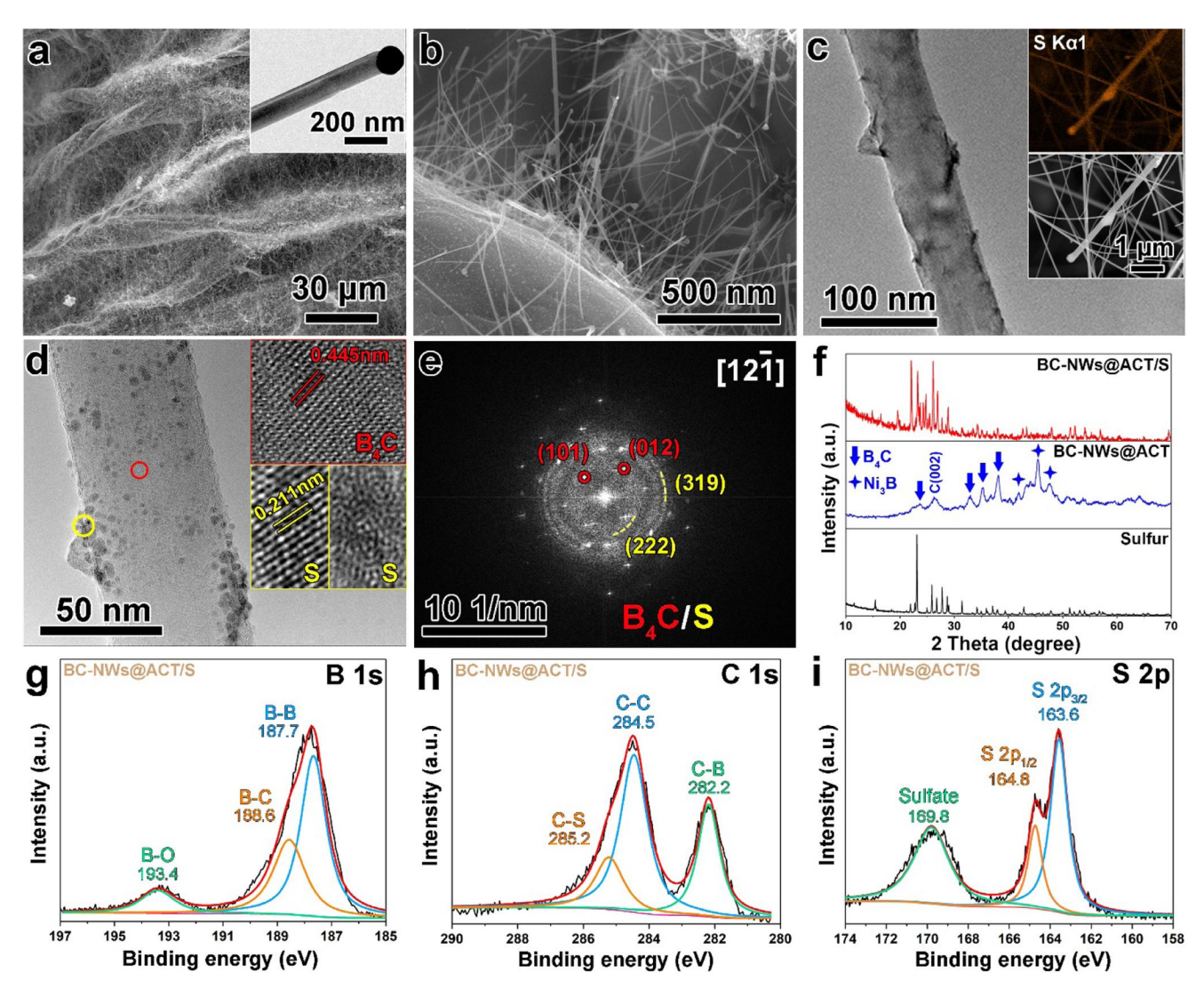


Fig. 2. Synthesis and characterization of BC-NWs@ACT/S composite. (a) Low-magnification SEM image of BC-NWs@ACT and TEM image inset of a B₄C nanowire. (b) SEM image of BC-NWs@ACT/S. (c) TEM image of BC-NW/S (EDS sulfur map and corresponding SEM image of BC-NWs/S in the inset). (d) HRTEM image and close-up observations of B₄C and sulfur, and (e) the corresponding FFT of BC-NW/S. (f) XRD patterns of sulfur powders, BC-NWs@ACT and BC-NWs@ACT/S. High-resolution (g) B 1s, (h) C 1s, and (i) S 2p XPS spectra of BC-NWs@ACT/S.

(CV) and electrochemical impedance spectroscopy (EIS) in the frequency ranging from $0.01\,Hz$ to $100\,kHz$ with an AC perturbation of $5\,mV$.

To characterize the inhibition effect of B_4C on polysulfide dissolution and diffusion, the as-synthesized BC-NWs@ACT/S composite was used as the cathode and assembled in a Li-S battery cell. After the assembled batteries were charged/discharged for several cycles, we stopped the tests during the charging process, and the coin batteries were disassembled manually. The cathodes were taken out and soaked into 1,2-dimethoxyethane (DME) to remove residual electrolyte and part of polysulfides. The as-obtained cathodes were further washed with acetone and dilute water, and then dried at 70 °C for 10 h. Visualized adsorption of polysulfide test was carried out using 1 mmol/ L Li₂S₆ solution in DIOX/DME (1:1, by volume). Li₂S₆ was synthesized by mixing lithium and sulfur at a molar ratio of 1:3 in DIOX/DME

2.4. MD simulations

All molecular dynamics (MD) calculations were performed using the Large-scale Atomic/Molecular Massively Parallel Simulator (LAMMPS) [46], to describe the response of BC-NWs@ACT/S/rGO hybrid structure to volume expansion and verify that boron carbide has an inhibitory

effect on "shuttle effect". The initial atomic configurations (boron carbide unit cell, graphene, lithium polysulfide, electrolyte molecules, Fig. S2) were optimized using Cambridge Serial Total Energy Package (CASTEP) [47] based on density functional theory (DFT). The generalized gradient approximation (GGA-PBE) was selected to describe exchange and correlation energy. The Broyden--Fletcher-Goldfarb-Shanno (BFGS) minimizer was used to perform cell optimization, and the convergence tolerance of total energy was set to be 1×10^{-6} eV/atom. The as-obtained configurations were replicated, truncated and combined to be the initial input structure for MD simulations. Periodic boundary conditions were applied in all directions. Boron carbide interactions were described by a set of Stillinger-Weber parameters [48]. The canonical ensemble (N, V, T) was applied to relax the structure with a time step of 0.25 fs, and the constant temperature was controlled by a Nose-Hoover thermostat method.

For the MD simulations of volume expansion, a cylindrical coreshell model was constructed with an inner diameter of 5 nm for B_4C core and an outer diameter of 10 nm for polysulfide nanoparticles. To be simplified, the cylindrical system was encapsulated by eight pieces of graphene sheet instead of rGO. Graphene was modeled by the adaptive intermolecular reactive empirical bond order (AIREBO) potential [49]. The non-bond interactions among B_4C , polysulfide nanoparticles and

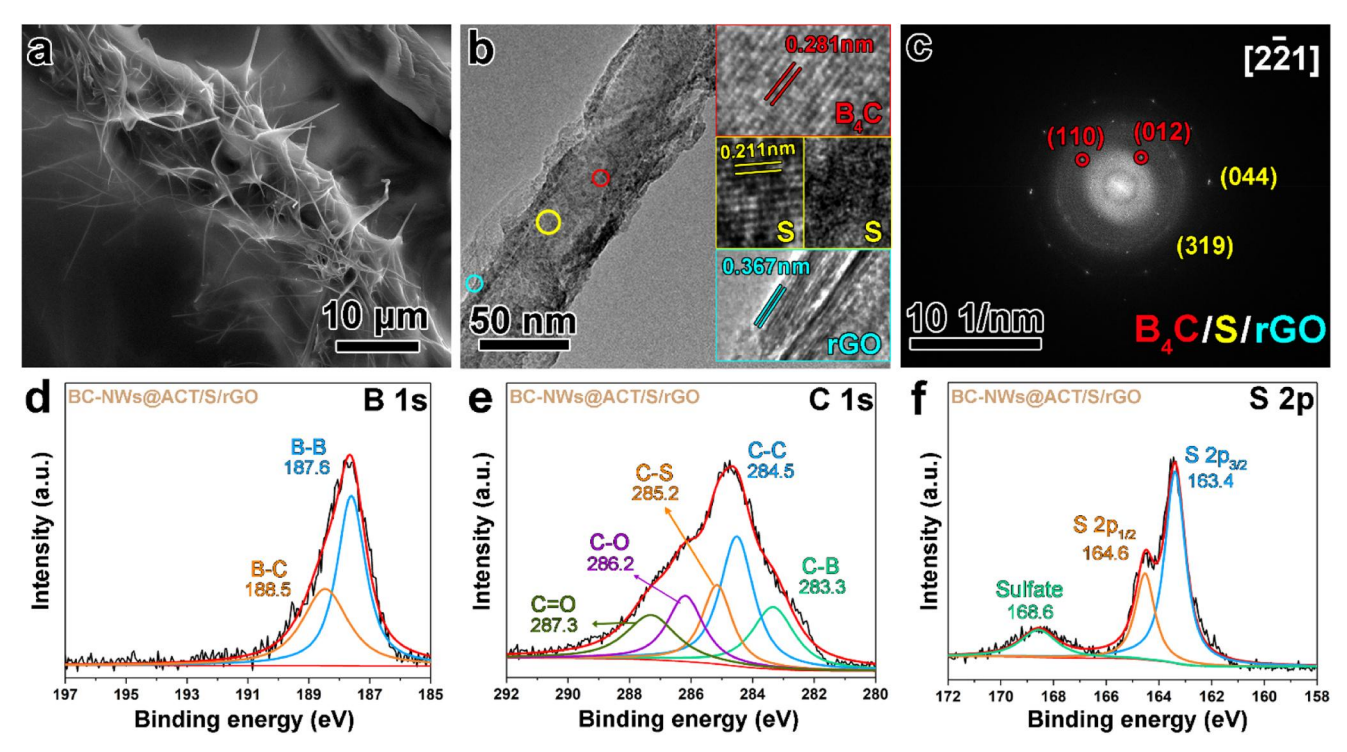


Fig. 3. Synthesis and characterization of BC-NWs@ACT/S/rGO composite. (a) SEM image of BC-NWs@ACT/S/rGO. (b) HRTEM image and close-up observations of B_4 C, sulfur and rGO, and (c) the corresponding FFT of BC-NWs/rGO. High-resolution (d) B 1s, (e) C 1s, and (f) S 2p XPS spectra of BC-NWs@ACT/S/rGO.

graphene were simply described by the Lennard-Jones (LJ) potential with parameters $\varepsilon = 1$ meV. Volume expansion and shrinkage processes were realized by varying parameter σ in LJ potential from 1 to 5 Å continuously [25]. Simulations temperature was set to be 1 K to ignore the thermal effect. For MD simulations of polysulfide dissolution and diffusion, the reactive force field simulation (ReaxFF) [50], with previously published Li/S ReaxFF parameter sets [51], was implemented to describe the Li/S interatomic interactions. Solvent molecules (1:1 mixture of DME and DIOX) were modeled using CHARMM force field [52], and the parameters are obtained from Ref [53,54] and [55]. The non-bond interactions were described by the LJ and Coulomb potential, and LJ parameters were simply set to be $\varepsilon = 1$ meV and $\sigma = 3$ Å, which are in the appropriate range for typical materials. After relaxed for 20000 MD steps, the atomic configurations were selected as the reference positions (x(0), Fig. 5f). The mean square displacement (MSD, $\langle [x(t) - x(0)]^2 \rangle$) of polysulfide particles was obtained as a function of time and the diffusion coefficient was calculated by linearly fitting the MSD-time curves.

3. Results and discussion

3.1. Synthesis and characterization of the electrode nanocomposite

A one-step synthesis (Fig. 1) was used to obtain BC-NWs@ACT hybrid structure via VLS method by utilizing amorphous boron powder as boron source, carbonaceous gases generated from pyrolysis of cotton as carbon source and nickel as the catalyst. Scanning electron microscopy (SEM) and transmission electron microscopy (TEM) images (Fig. 2a) demonstrate that high-density boron carbide nanowires with catalytic particles on their tips are uniformly aligned on ACT microfibers. Each 1 $\mu m \times 1~\mu m$ region contains around 20 nanowires, which have dimensions with diameters in the range of 50–500 nm and the average length of 5 μm . X-ray diffraction (XRD) analysis verifies that the nanowires are rhombohedral boron carbide (JCPDS No. 6–0555) with nickel boride in the catalyst particles (Fig. 2f). Typical peak broadening and shifting are due to the existence of nickel and small

particle sizes [56]. The nitrogen absorption/desorption test showed that such BC-NWs@ACT composite had a BET surface area of \sim 142.6 m²/g (Fig. S3).

Afterward, sulfur was deposited via a simple melt-diffusion method at 156 °C to construct the BC-NWs@ACT/S nanocomposite, Fig. 2b.c show the SEM image of BC-NWs@ACT/S and the TEM image of an individual B₄C nanowire coated with sulfur. No obvious morphology changes are observed after heating but the surface of the nanowire becomes "rougher" due to the uniform deposition of sulfur, which is further verified by energy dispersive X-ray (EDX) spectrum (Fig. S4) and sulfur elemental mapping (the insets of Fig. 2c). The primary structural unit cell of B₄C (Fig. S2) exhibited a rhombohedral arrangement consisting of 12-atom icosahedra and 3-atom linear chains $(R\overline{3}m \text{ space group}, a=5.16 \text{ Å}, \text{ and } \alpha=65.7^{\circ})$ [33]. A close-up inspection (Fig. 2d) and the corresponding Fast Fourier Transform (FFT) pattern with a zone axis $[12\overline{1}]$ (Fig. 2e) indicate that the B₄C nanowires were grown with the perfect rhombohedral crystal lattice, and clearly demonstrate that sulfur particles were homogeneously anchored on the surface of nanowires. The measured crystal plane spacings of B₄C are consistent with the (101) and (012) reflections in the XRD patterns (Fig. 2f). The high resolution TEM (HRTEM) images (the insets of Fig. 2d) and the diffraction rings (broad and narrow) in Fig. 2e jointly verify that sulfur existed in both polycrystalline and amorphous phases. The lattice fringe spacing of ~0.211 nm is uniquely indexed to the (319) crystal plane of sulfur in the orthorhombic structure, in good agreement with the XRD results in Fig. 2f (JCPDS no. 08-0247). X-ray photoelectron spectroscopy (XPS) was performed to detect the elemental composition and the chemical bonding states of BC-NWs@ACT/ S. In the B 1s spectra, three peaks centered at 187.7, 188.6, and 193.4 eV were observed, corresponding to B-B, B-C, and B-O bonds respectively (Fig. 2g). The C 1s peaks revealed the existence of C-B (282.2 eV), C-C (284.5 eV), and C-S (285.2 eV) bonds (Fig. 2h) [57]. The S 2p spectrum was deconvoluted into three peaks centered at 163.6 eV (S 2p_{3/2}), 164.8 eV (S 2p_{1/2}), and 169.8 eV (Sulfate) (Fig. 2i). The S $2p_{3/2}$ and S $2p_{1/2}$ peaks have an energy separation of 1.2 eV and intensity ratio of 2:1, confirming the successful loading of sulfur [58].

With various functional groups on the surface (epoxy and hydroxyl groups), GO has been reported as a polysulfide immobilizer which can slow down the diffusion and prevent the parasitic reactions on electrodes [59]. Herein, to further mitigate the shuttle effect, the as-obtained BC-NWs@ACT/S nanocomposite was wrapped with partially reduced GO sheets. The SEM image of BC-NWs@ACT/S/rGO (Fig. 3a) reveals that the ACT microfiber with radially growing B₄C nanowires as branches was wrapped by the silk-like rGO skin, and the individual nanowire was also uniformly covered by the compact self-assembled rGO sheets (Fig. 3b). The enlarged HRTEM images (the insets of Fig. 3b) and the corresponding FFT pattern (Fig. 3c) present that B_4C nanowires remained well single crystal lattice structure after the heating treatment up at 200 °C and can retain excellent mechanical properties. Raman spectrum was used to characterize the surface components (Fig. S5) of BC-NWs@ACT/S/rGO electrode. For untreated BC-NWs@ACT samples, Raman peaks in the range of 200-600 cm⁻¹ are assigned to the vibrations of chain structures of B₄C, and the regions above 600 cm⁻¹ are associated with intraicosahedral and intericosahedral modes [60]. The sharp peaks in the Raman spectrum ranging from 100 to 500 cm⁻¹ appear in the BC-NWs@ACT/S sample and vanish in the BC-NWs@ACT/ S/rGO sample, suggesting that sulfur is well dispersed and confined by rGO protective shell. The successful loading of sulfur was further confirmed by high-resolution S 2p XPS analysis of BC-NWs@ACT/S/rGO, showing the S $2p_{3/2}$ and S $2p_{1/2}$ peaks with energy separation of 1.2 eV and intensity ratio of 2:1 (Fig. 3f). In the B 1s spectra, the two dominant peaks centered at 187.6 and 188.5 eV were identified as B-B and B-C bonds, respectively (Fig. 3d). The C 1s spectrum was deconvoluted into five peaks at 283.3, 284.5, 285.2, 286.2, and 287.3 eV, which can be ascribed to C-B, C-C, C-S, C-O (hydroxyl and epoxy groups), and O = C-O=(carboxyl groups) bonds, respectively (Fig. 3e). The results are consistent with the previous studies [57,61]. In sum, the BC-NWs@ACT scaffold was successfully fabricated, anchored by sulfur and enfolded by rGO skin, which acts as a natural barrier to polysulfide diffusion. The B₄C nanowires and rGO sheets jointly maximize the interfacial contacts between sulfur and the cathode where the electrochemical redox reaction occurs. Furthermore, the mechanically strong B₄C skeleton and rGO skin are expected to buffer the volume variations and thereby enhance the cyclic stability.

3.2. Electrochemical characterization

CR2032 type coin cells were fabricated using the BC-NWs@ACT/S/ rGO nanocomposite (Fig. 4a) as the freestanding cathode and Li foil as the anode for electrochemical performance evaluation. Bare ACT/S, ACT/S/rGO, and BC-NWs@ACT/S electrodes were also assembled in coin cells for comparison. The sulfur loading of the cathodes was measured to be $\sim 3.0 \text{ mg/cm}^2$. Fig. S6a shows the galvanostatic voltage profiles of the battery at the current density of 0.6 mA/cm² with a voltage window between 1.3 and 3 V. The profiles of ACT/S and ACT/ S/rGO cells display a typical two-plateau discharging morphology which corresponds to the reduction of S₈ molecule to long-chain dissolved polysulfides (Li₂S_x, $4 \le x \le 8$) and the subsequent formation of short-chain insoluble polysulfides (Li₂S₂, Li₂S), respectively [14]. Intriguingly, BC-NWs@ACT/S and BC-NWs@ACT/S/rGO electrodes (Fig. 4c) exhibited a sloping discharge plateau in the galvanostatic charge/discharge curves at the current density of 0.6 mA/cm². The cyclic voltammetry (CV) curves obtained at a sweep rate of 0.1 mV/s (Fig. 4b) confirmed this finding. Theoretically, the Li-S battery features two cathodic peaks, corresponding to the transformations of S_8 to $-S_4^{2}$ and -S₄²⁻ to -S²⁻, respectively. Unexpectedly, the BC-NWs@ACT/S/rGO cell exhibited a single pair of redox peaks, with the oxidation peak at $2.68\,V$ versus Li $^+/Li$ and the reduction peak at $2.18\,V$ versus Li $^+/Li$, indicating that the dissolution of polysulfides was disrupted by the existence of BC-NWs. During the first 300 cycles, the overall features of the charge/discharge curves show no obvious changes, implying good electrochemical stability of the BC-NWs@ACT/S/rGO cathode and highly reversible redox reactions. Comparing with other control samples (Fig. S6b), the BC-NWs@ACT/S/rGO electrode showed almost negligible overcharging behavior in the first cycle, indicating that the polysulfide shuttle effect was significantly reduced [62].

The rate capability of the BC-NWs@ACT/S/rGO composite is displayed in Fig. 4d. Theoretically, a lower capacity is often obtained at a higher rate due to polarization. Intriguingly, with increasing current rate from 0.1 to 1.2 mA/cm², the capacity of the BC-NWs@ACT/S/rGO cell initially increased and then gradually decreased afterward, because sulfur utilization gradually enhanced in this hybrid structured electrode. The reversible discharge capacities delivered by the battery are 1166, 1195, 1008, 890, 833 and 805 mAh/g at the current rates of 0.1, 0.2, 0.4, 0.6, 1.0 and $1.2 \,\mathrm{mA/cm^2}$, respectively. At the maximum charge/discharge rate (1.2 mA/cm²), the cycling process remained stable with a high specific capacity (~800 mAh/g). Impressively, when the current rate was reversed to 0.6 mA/cm², the discharge capacity recovered and even increased continuously up to 965 mAh/g over 50 cycles, demonstrating an excellent rate capability. The long-term cycling test was carried out to further characterize the electrochemical properties of the BC-NWs@ACT/S/rGO electrode, which exhibited an outstanding cycling performance at a high current density of 1.5 mA/ cm² for over 1000 charge/discharge cycles (Fig. 4e). The initial discharge capacity is 963 mAh/g and the discharge capacity increased gradually up to 1395 mAh/g in the first 50 cycles due to the increasing utilization of sulfur in the 3D hybrid structural electrode [63]. A high specific capacity retention of 89.8% was achieved at the 400th cycle and an ultralow capacity loss rate of 0.056% per cycle was obtained for 1000 cycles, revealing that the shuttle effect was significantly reduced via the spatial and chemical confinement enabled by the three-dimensional BC-NWs@ACT/S/rGO structure. Additionally, the cell presented a coulombic efficiency as high as 95.4% even after 1000 cycles, and the average coulombic efficiency was calculated to be 97.4%, illustrating superior sulfur utilization and cyclic stability of BC-NWs@ACT/S/rGO. For comparison, the cycling performances of ACT/S, ACT/S/rGO, and BC-NWs@ACT/S were also characterized (Fig. S6b). The profile of ACT/S displayed an initial discharge capacity of 914 mAh/g, which is close to that of BC-NWs@ACT/S/rGO electrode due to the same sulfur loading. However, the capacity of ACT/S faded rapidly down to 292 mAh/g after 700 cycles with 0.1% capacity loss per cycle. The specific capacity retention of ACT/S/rGO and BC-NWs@ACT/S electrodes were calculated to be 91.2% and 90.1% at the 400th cycle, respectively. indicating the inhibitory effect of both BC-NWs and rGO on "shuttle effect". The lifespan verified that hierarchically configured BC-NWs@ACT/S/rGO cathode can largely enhance the cycling stability. The electrochemical impedance spectra (EIS) of the BC-NWs@ACT/S/ rGO cell at the 1st and 500th cycles are shown in Fig. S7. The Nyquist plots are composed of two depressed semicircles and a straight line. The semicircle in the high-frequency range corresponds to the formation of the passivation layer (Li₂S₂/Li₂S) on the surface of the lithium anode (R₂), and the semicircle in the middle-frequency range attributes to the Li ⁺ charge transfer (R₃). The straight line in the low-frequency region relates to the diffusion of lithium ions. Based on the equivalent circuit fitting, after cycling, R₂ increased, suggesting the formation of SEI film. Meanwhile, the slight increase of charge transfer resistance after 500 cycles indicated that the BC-NWs@ACT/S/rGO cathode was stable after long time cycling. Impressively, armed with the B₄C nanoskeleton and rGO skin, the BC-NWs@ACT/S/rGO cathode exhibited superior electrochemical performance - higher specific capacity, longer cycling life and greater rate capability.

3.3. Role of BC-NWs and rGO in Li-S cell

The immobilizing effect of rGO on sulfur and lithium polysulfides via the reactive functional groups has been extensively studied [59]. However, to the best of our knowledge, no previous studies have been reported on the inhibition effect of B_4C on polysulfide dissolution and

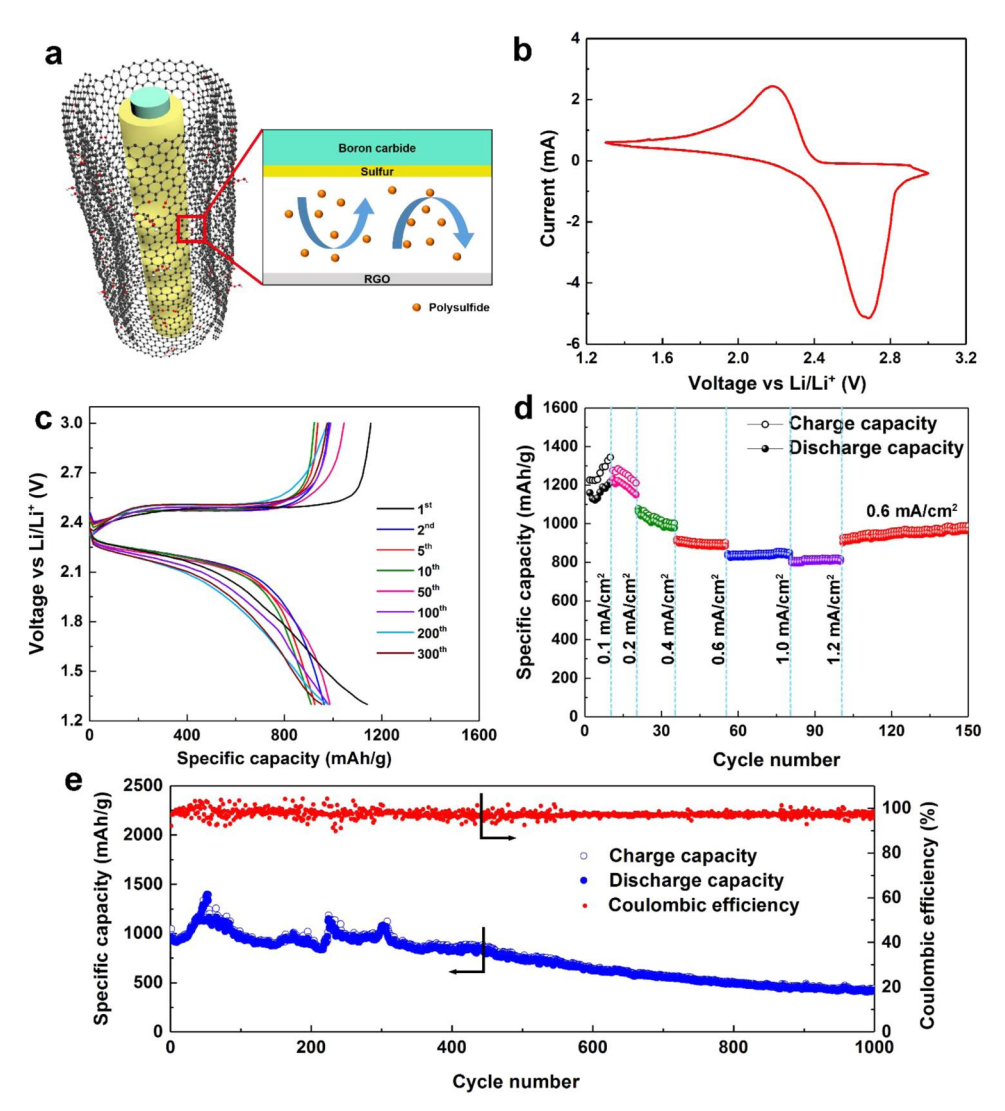


Fig. 4. Electrochemical characterization of BC-NWs@ACT/S/rGO composite electrode. (a) Schematic illustration of a representative volume element of BC-NWs@ACT/S/rGO electrode. (b) Initial cyclic voltammogram profiles at a scan rate of 0.1 mV/s. (c) Galvanostatic discharge/charge profiles at the current density of 0.6 mA/cm². (d) Rate performance at different current densities. (e) Cycling performance and correlated coulombic efficiency.

diffusion. In this work, both experimental characterizations and molecular dynamics (MD) simulations were carried out to unveil the role of B₄C nanowires in Li-S batteries. To rule out the impact of rGO skin, sulfur powders were loaded onto the bare BC-NWs@ACT plate without coating rGO. The as-synthesized BC-NWs@ACT/S composite was then used as the cathode and assembled in a Li-S battery cell. After 10 cycles of charge/discharge, the cell was disassembled to characterize the morphological changes of the cycled cathode by SEM. The cycled BC-NWs@ACT/S and ACT/S (the control sample) cathodes were rinsed with 1,2- dimethoxyethane (DME), acetone and distilled water to compare the capacities of polysulfide adsorption. At the same magnification, SEM inspections on the cycled BC NWs@ACT/S (Fig. 5a) and ACT/S (Fig. 5c) samples present that individual BC-NWs@ACT microfibers have an average diameter of 16.5 µm, which is much larger than the pristine ACT fibers (5.4 µm), indicating that large amounts of polysulfides are anchored on the BC-NWs@ACT/S cathode. Compared with the ACT/S sample (Fig. 5d), the B₄C nanoskeleton in the BC-NWs@ACT/S cathode largely enhanced the surface area of the cathode, hindering the dissolution of polysulfides (Fig. 5b). Static polysulfide absorption test (Fig. 5e) was carried out to further evaluate the adsorption capability of B₄C, with the solution of 1 mmol/L Li₂S₆ in 1,3dioxolane (DIOX)/1,2- dimethoxyethane (DME) (1:1, by volume). No obvious color change was observed for the Li₂S₆ solution with ACT,

indicating a weak absorption capability. Compared with ACT, the significant color fading (brown to colorless) of the Li_2S_6 solution with BC-NWs@ACT suggested the strong interactions between B_4C and polysulfides.

MD simulations were carried out to further uncover how B_4C nanowires affect the polysulfide diffusion process in the electrolyte (Fig. 5f, and Fig. S2). The diffusion coefficient of polysulfide molecules, D_f , was calculated at room temperature through

$$D_f = \lim_{x \to \infty} \langle [x(t) - x(0)]^2 \rangle / 2t \tag{1}$$

where t is time, $\langle [x(t)-x(0)]^2 \rangle$ is the mean square displacement (MSD) of polysulfide molecules in direction x. The drift of the center of mass (COM) of polysulfides was subtracted out before MSD was calculated. At room temperature (300 K), D_f of polysulfides in the electrolyte without B₄C was obtained as 1.87×10^{-10} m²/s, which is consistent with previous work [64,65]; while the B₄C nanoskeleton successfully reduced the diffusivity down to 1.06×10^{-10} m²/s, revealing that the B₄C nanowires can effectively confine the polysulfide particles around the cathode, and largely limit the shuttle effect, in accord with the experimental results. In our model, the interaction between B₄C and polysulfides is only described by van der Waals forces (LJ potential, Coulombic interaction). In nanowire growth, amorphous carbon

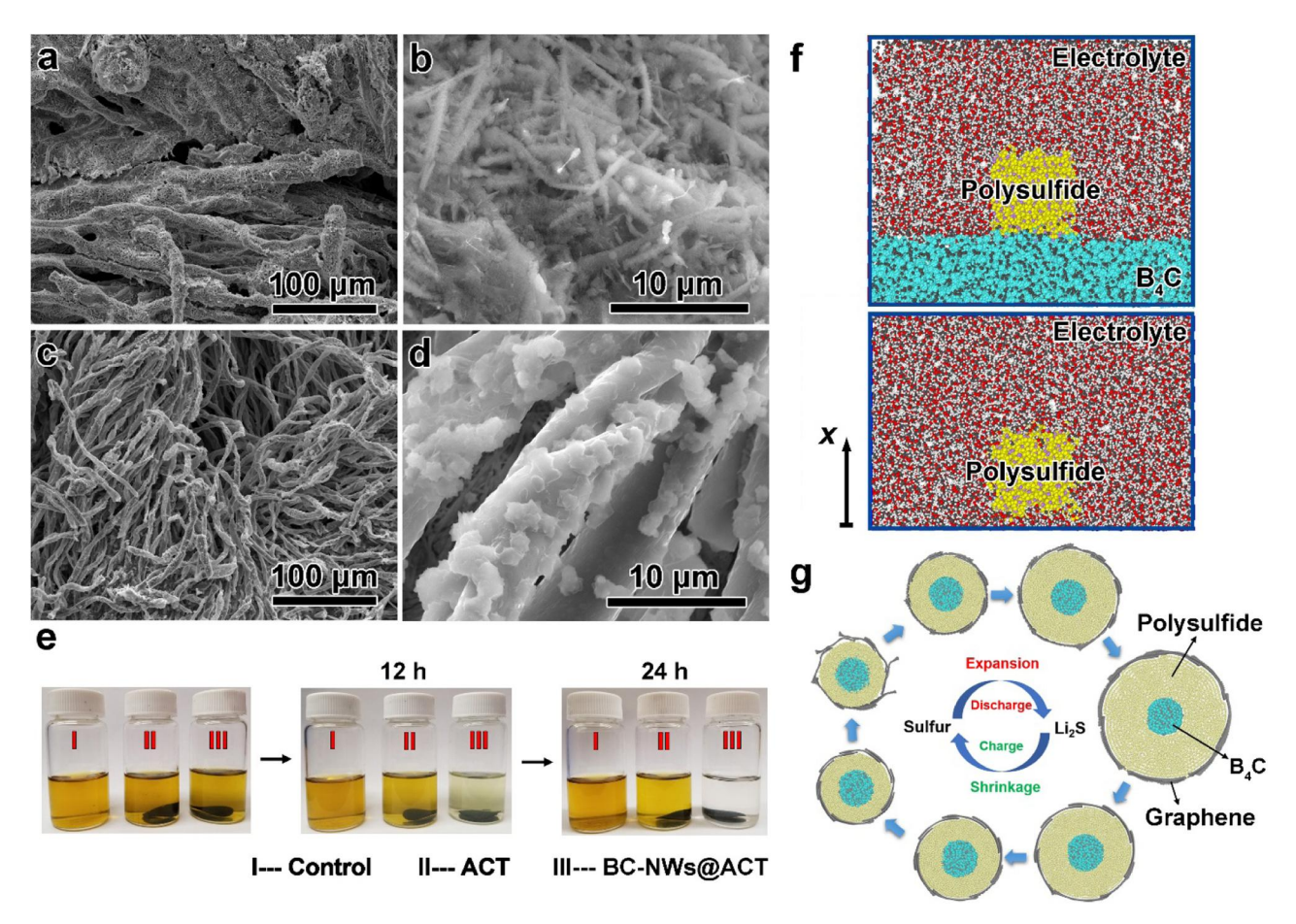


Fig. 5. SEM images of (a,b) BC-NWs@ACT/S and (c,d) ACT/S electrodes after cycling. (e) Photographs of Li_2S_6 polysulfide absorption test with ACT and BC-NWs@ACT. (f) MD models of polysulfide particle diffusion with and without B_4C . (g) MD snapshots of the atomic configurations representing a cross-section of the BC-NWs/S/graphene cylindrical structure in a cycle of charge/discharge process.

coating with functional groups could be generated, which could further absorb polysulfides via chemical bonding.

In addition to the shuttle effect, the large volume variation during charge/discharge process is another factor that deteriorates the electrochemical performance of Li-S batteries. To simplify the system, for MD simulations graphene sheets were studied instead of rGO. The atomic configuration (Fig. 5g) represents a cross-section of a typical representative volume element (RVE) of the BC-NWs/S/graphene cylindrical structure, based on which MD simulations were performed to investigate the self-adaptive behavior to the volume change of graphene skin during the discharge/charge process. The MD results reveal that the B₄C core remains stable while the graphene shell accommodates a large volume change without destructing the structure. In a cycle of polysulfide expansion/contraction, the multilayer graphene unfolds and slides back and forth between layers while maintaining contact with the internal polysulfide structure, which can release strain energy induced by volume variations and enhance the charge transfer kinetics. In reality, the self-adaptive process of the BC-NWs@ACT/S/ rGO electrode should be more complicated due to its complex hybrid structure. Therefore, the capacity changes, in the first 300 cycles, were induced by the gradual utilization of sulfur and the complex selfadaptive behavior of cathode (Fig. 4e). After the self-optimization process, the BC-NWs@ACT/S/rGO cell became much stable, thus largely increasing its lifespan. Armed with an in-depth understanding of the experimental results and MD simulations, it is concluded that the synergistic effects of B₄C nanoskeleton and rGO skin largely enhance the electrode stability, thereby improving the electrochemical performance. This BC-NWs@ACT/S/rGO configuration demonstrates unprecedented opportunities for designing robust cathodes for Li-S batteries.

3.4. Flexible lithium-sulfur batteries with BC-NWs@ACT/S/rGO cathode

A flexible cell was assembled with the BC-NWs@ACT/S/rGO as a cathode, Celgard 2400 film as a separator and lithium foil as an anode. No external pressure was applied during the assembling process. Charge/discharge cycling tests (Fig. 6a) were carried out to characterize the electrochemical properties of the flexible BC-NWs@ACT/S/ rGO electrode at normal (1st-25th cycles) and bent (25th-50th cycles) states. The flexible cell was cycled in normal state from the beginning, and the capacity was found to be stabilized at ~500 mAh/g under the bent state, because in the bent state, external pressure was applied, thereby improving the solid-solid interfacial contact. Similarly, the flexible cell displays a sloping discharge plateau in the galvanostatic charge/discharge curves under normal (1st, 2nd and 3rd cycles) and bent (25th, 26th, and 27th cycles) states (Fig. 6b). The reproducible charge/discharge voltage profiles together with the negligible overcharging behavior in the initial cycle unveil that the flexible BC-NWs@ACT/S/rGO electrode possesses excellent mechanical robustness and electrochemical stability. A light-emitting diode (LED) was lightened up by the as-obtained soft package Li-S cell at flat and folded states (Fig. 6c), verifying the practicality of the flexible BC-NWs@ACT/ S/rGO cathode. To characterize the mechanical properties and chemical stability of BC-NWs, the flexible BC-NWs@ACT/S/rGO cathodes, before and after cycling, were treated by ultrasonication, to separate and disperse BC-NWs onto the silicon substrate. The nanoindentation forcedisplacement curves obtained from the BC-NWs before and after cycling are almost identical (Fig. 6d), demonstrating that battery cycling and

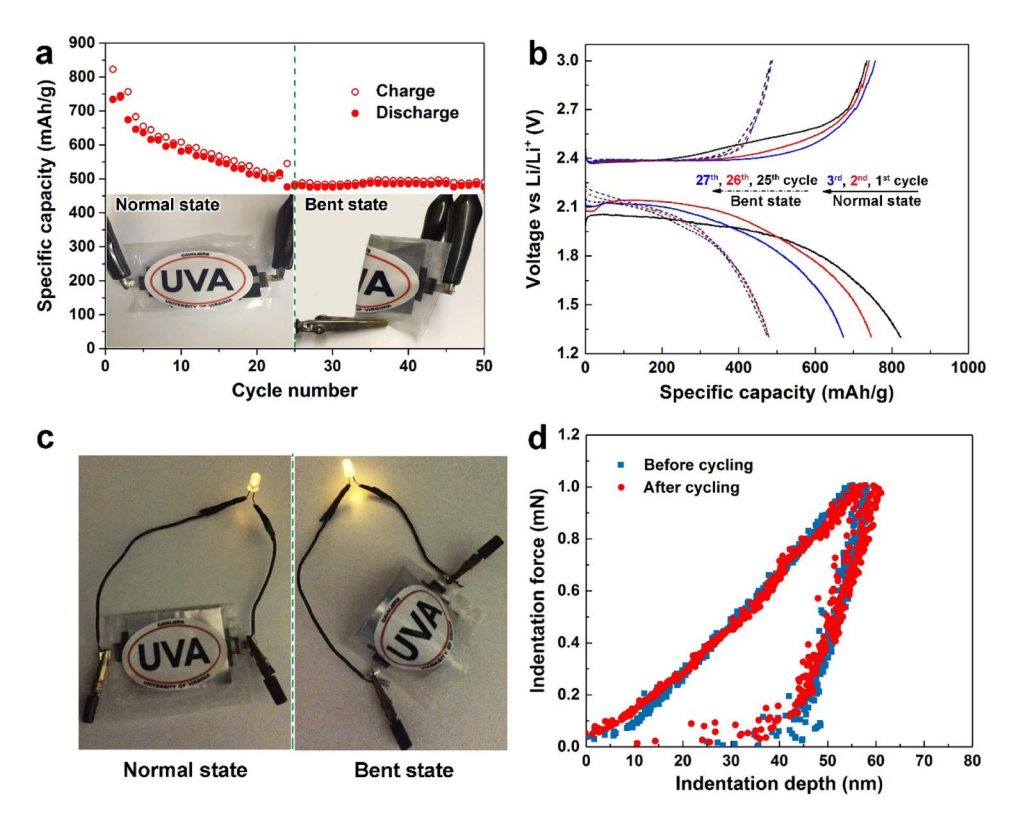


Fig. 6. Electrochemical performance and mechanical characterization of the flexible BC-NWs@ACT/S/rGO composite electrode. (a) Cyclic performance of the flexible battery cell under normal and bent states. (b) The charge/discharge voltage profiles under normal (1st, 2nd and 3rd cycles) and bent (25th, 26th, and 27th cycles) states. (c) The photograph of soft package Li-S cell lightening up a light-emitting diode (LED) in normal and bent states. (d) Nanoindentation load-displacement curves of BC-NWs before and after cycling.

complex chemical environment have little effect on the mechanical properties of BC-NWs. The reduced elastic moduli were measured to be 253 and 226 GPa before and after over 1000 cycles, respectively, based on the unloading curves according to the Oliver-Pharr method [66]. Convincingly, BC-NWs@ACT hybrid structure is a promising candidate in the flexible energy storage devices due to the flexibility of ACT, excellent mechanical properties and chemical stability of BC-NWs.

4. Conclusion

In summary, the flexible ACT cloth with boron carbide nanowires as the skeleton and reduced graphene oxide as the protective skin was successfully synthesized via low-cost raw materials and employed as a 3D conductive host for sulfur to construct high performance flexible lithium-sulfur batteries. Compared with the ACT/S electrode, the asfabricated Li-S battery using BC-NWs@ACT/S/rGO as the cathode demonstrated the combined advantages of ACT, B₄C nanowires and rGO, and yielded significant improvements, in terms of high specific capacity (the initial discharge capacity was 963 mAh/g and after 50 cycles increased to 1395 mAh/g at a high current density of 1.5 mA/cm²), superior cycling stability (over 1000 cycles), ultralow capacity decay rate (0.056% per cycle) and excellent rate capability (current density from 0.1 to 1.2 mA/cm²). The excellent electrochemical performance of BC-NWs@ACT/S/rGO cell was primarily attributed to the outstanding mechanical properties of the B₄C skeleton, the self-adaptive capability to volume variations of rGO skin, and the synergistic effects of B₄C and rGO on the suppression of polysulfide diffusion. The flexible freestanding BC-NWs@ACT/S/rGO cathode was also assembled into a foldable Li-S cell, presenting a high specific capacity and excellent mechanical stability. Such novel B₄C nanowire enabled electrode system opens up unprecedented opportunities for designing flexible high-performance energy storage devices.

Acknowledgements

Financial support for this study was provided by the U.S. National

Science Foundation (CMMI-1728042). The authors thank the staff members at the University of Virginia NMCF for electron microscopy technical support.

Conflict of interest

The authors declare no conflict of interest.

Appendix A. Supporting information

Supplementary data associated with this article can be found in the online version at doi:10.1016/j.nanoen.2019.01.018.

References

- [1] M. Armand, J.-M. Tarascon, Building better batteries, Nature 451 (2008) 652–657, https://doi.org/10.1038/451652a.
- [2] B. Dunn, H. Kamath, J.-M. Tarascon, Electrical energy storage for the grid: a battery of choices, Science 334 (2011) 928–935, https://doi.org/10.1126/science. 1212741.
- [3] L. Yan, H. Wang, D. Huang, H. Luo, Electrodes with high conductivities for high performance lithium/sodium ion batteries, Eng. Sci. (2018) 4–20, https://doi.org/ 10.30919/es.180318.
- [4] R. Li, C. Lin, N. Wang, L. Luo, Y. Chen, J. Li, Z. Guo, Advanced composites of complex Ti-based oxides as anode materials for lithium-ion batteries, Adv. Compos. Hybrid. Mater. 1 (2018) 440–459, https://doi.org/10.1007/s42114-018-0038-1.
- [5] J.B. Goodenough, Y. Kim, Challenges for rechargeable Li batteries, Chem. Mater. 22 (2010) 587–603, https://doi.org/10.1021/cm901452z.
- [6] X. Lou, C. Lin, Q. Luo, J. Zhao, B. Wang, J. Li, Q. Shao, X. Guo, N. Wang, Z. Guo, Crystal structure modification enhanced FeNb₁₁O₂₉ anodes for Lithium-Ion batteries, ChemElectroChem 4 (2017) 3171–3180, https://doi.org/10.1002/celc. 201700816.
- [7] X.-C. Zhao, P. Yang, L.-J. Yang, Y. Cheng, H.-Y. Chen, H. Liu, G. Wang, V. Murugadoss, S. Angaiah, Z. Guo, Enhanced electrochemical performance of Cu²⁺ doped TiO₂ nanoparticles for Lithium-ion battery, ES Mater. Manuf. (2018) 67–71, https://doi.org/10.30919/esmm5f109.
- [8] C. Lin, L. Hu, C. Cheng, K. Sun, X. Guo, Q. Shao, J. Li, N. Wang, Z. Guo, Nano-TiNb₂O₇/carbon nanotubes composite anode for enhanced lithium-ion storage, Electrochim. Acta 260 (2018) 65–72, https://doi.org/10.1016/j.electacta.2017.11
- [9] J. Tian, Q. Shao, X. Dong, J. Zheng, D. Pan, X. Zhang, H. Cao, L. Hao, J. Liu, X. Mai, Z. Guo, Bio-template synthesized NiO/C hollow microspheres with enhanced Li-ion battery electrochemical performance, Electrochim. Acta 261 (2018) 236–245,

- https://doi.org/10.1016/j.electacta.2017.12.094.
- [10] Q. Pang, X. Liang, C.Y. Kwok, L.F. Nazar, Advances in lithium-sulfur batteries based on multifunctional cathodes and electrolytes, Nat. Energy 1 (2016) 1–11, https://doi.org/10.1038/nenergy.2016.132.
- [11] P.G. Bruce, S.A. Freunberger, L.J. Hardwick, J.-M. Tarascon, Li-O₂ and Li-S batteries with high energy storage, Nat. Mater. 11 (2012) 19–29, https://doi.org/10.1038/nmat3191.
- [12] H. Wang, Y. Yang, Y. Liang, J.T. Robinson, Y. Li, A. Jackson, Y. Cui, H. Dai, Graphene-wrapped sulfur particles as a rechargeable lithium-sulfur battery cathode material with high capacity and cycling stability, Nano Lett. 11 (2011) 2644–2647, https://doi.org/10.1021/nl200658a.
- [13] Y. Yang, G. Zheng, Y. Cui, Nanostructured sulfur cathodes, Chem. Soc. Rev. 42 (2013) 3018–3032, https://doi.org/10.1039/c2cs35256g.
- [14] M. Wild, L. O'Neill, T. Zhang, R. Purkayastha, G. Minton, M. Marinescu, G.J. Offer, Lithium sulfur batteries, a mechanistic review, Energy Environ. Sci. 8 (2015) 3477–3494, https://doi.org/10.1039/C5EE01388G.
- [15] A. Manthiram, Y. Fu, S. Chung, C. Zu, Y. Su, Rechargeable lithium sulfur batteries, Chem. Rev. 114 (2014) 11751–11787, https://doi.org/10.1021/cr500062v.
- [16] Y. Zhang, L. Qian, W. Zhao, X. Li, X. Huang, X. Mai, Z. Wang, Q. Shao, X. Yan, Z. Guo, Highly efficient Fe-N-C nanoparticles modified porous graphene composites for oxygen reduction reaction, J. Electrochem. Soc. 165 (2018) H510–H516, https://doi.org/10.1007/BF02812637.
- [17] Q. Luo, H. Ma, F. Hao, Q. Hou, J. Ren, L. Wu, Z. Yao, Y. Zhou, N. Wang, K. Jiang, H. Lin, Z. Guo, Carbon nanotube based inverted flexible perovskite solar cells with all-inorganic charge contacts, Adv. Funct. Mater. 27 (2017) 1–8, https://doi.org/10.1002/adfm.201703068.
- [18] B. Kirubasankar, V. Murugadoss, J. Lin, T. Ding, M. Dong, H. Liu, J. Zhang, T. Li, N. Wang, Z. Guo, S. Angaiah, In situ grown nickel selenide on graphene nanohybrid electrodes for high energy density asymmetric supercapacitors, Nanoscale 10 (2018) 20414–20425, https://doi.org/10.1039/c8nr06345a.
- [19] Q. Luo, H. Ma, Q. Hou, Y. Li, J. Ren, X. Dai, Z. Yao, Y. Zhou, L. Xiang, H. Du, H. He, N. Wang, K. Jiang, H. Lin, H. Zhang, Z. Guo, All-carbon-electrode-based endurable flexible perovskite solar cells, Adv. Funct. Mater. 28 (2018) 1–8, https://doi.org/ 10.1002/adfm_201706777.
- [20] T. Liu, K. Yu, L. Gao, H. Chen, N. Wang, L. Hao, T. Li, H. He, Z. Guo, A graphene quantum dot decorated SrRuO3mesoporous film as an efficient counter electrode for high-performance dye-sensitized solar cells, J. Mater. Chem. A 5 (2017) 17848–17855, https://doi.org/10.1039/c7ta05123a.
- [21] H. Liu, M. Dong, W. Huang, J. Gao, K. Dai, J. Guo, G. Zheng, C. Liu, C. Shen, Z. Guo, Lightweight conductive graphene/thermoplastic polyurethane foams with ultrahigh compressibility for piezoresistive sensing, J. Mater. Chem. C 5 (2017) 73–83, https://doi.org/10.1039/c6tc03713e.
- [22] H. Liu, Y. Li, K. Dai, G. Zheng, C. Liu, C. Shen, X. Yan, J. Guo, Z. Guo, Electrically conductive thermoplastic elastomer nanocomposites at ultralow graphene loading levels for strain sensor applications, J. Mater. Chem. C 4 (2015) 157–166, https:// doi.org/10.1039/c5tc02751a.
- [23] Z. Gao, Y.Y. Zhang, N.N. Song, X.D. Li, Towards flexible lithium-sulfur battery from natural cotton textile, Electrochim. Acta 246 (2017) 507–516, https://doi.org/10. 1016/j.electacta.2017.06.069.
- [24] J. Guo, Y. Xu, C. Wang, Sulfur-impregnated disordered carbon nanotubes cathode for lithium sulfur batteries, Nano Lett. (2011) 4288–4294, https://doi.org/10. 1021/nl202297p.
- [25] Y. Zhao, J. Feng, X. Liu, F. Wang, L. Wang, C. Shi, L. Huang, X. Feng, X. Chen, L. Xu, M. Yan, Q. Zhang, X. Bai, H. Wu, L. Mai, Self-adaptive strain-relaxation optimization for high-energy lithium storage material through crumpling of graphene, Nat. Commun. 5 (2014) 1–8, https://doi.org/10.1038/ncomms5565.
- [26] Y.Y. Zhang, F.M. Heim, N.N. Song, J.L. Bartlett, X.D. Li, New insights into mossy Li induced anode degradation and its formation mechanism in Li-S batteries, ACS Energy Lett. 2 (2017) 2696–2705, https://doi.org/10.1021/acsenergylett.7b00886.
- [27] Y.Y. Zhang, Z. Gao, X.D. Li, Capillarity composited recycled paper/graphene scaffold for lithium-sulfur batteries with enhanced capacity and extended lifespan, Small 1701927 (2017) 1–12, https://doi.org/10.1002/smll.201701927.
- [28] Z. Wei Seh, W. Li, J.J. Cha, G. Zheng, Y. Yang, M.T. McDowell, P.-C. Hsu, Y. Cui, Sulphur-TiO₂ yolk-shell nanoarchitecture with internal void space for long-cycle lithium-sulphur batteries, Nat. Commun. 4 (2013) 1331, https://doi.org/10.1038/ ncomms2327.
- [29] Q. Pang, D. Kundu, M. Cuisinier, L.F. Nazar, Surface-enhanced redox chemistry of polysulphides on a metallic and polar host for lithium-sulphur batteries, Nat. Commun. 5 (2014) 4759, https://doi.org/10.1038/ncomms5759.
- [30] X. Wang, G. Li, J. Li, Y. Zhang, A. Wook, A. Yu, Z. Chen, Structural and chemical synergistic encapsulation of polysulfides enables ultralong-life lithium–sulfur batteries, Energy Environ. Sci. 9 (2016) 2533–2538, https://doi.org/10.1039/ C6EE00194G.
- [31] X. Xia, Y. Zhang, D. Chao, Q. Xiong, Z. Fan, X. Tong, J. Tu, H. Zhang, H.J. Fan, Tubular TiC fibre nanostructures as supercapacitor electrode materials with stable cycling life and wide-temperature performance, Energy Environ. Sci. 8 (2015) 1559–1568, https://doi.org/10.1039/C5EE00339C.
- [32] J.T. Lee, Y. Zhao, S. Thieme, H. Kim, M. Oschatz, L. Borchardt, A. Magasinski, W. Il Cho, S. Kaskel, G. Yushin, Sulfur-infiltrated micro- and mesoporous silicon carbidederived carbon cathode for high-performance lithium sulfur batteries, Adv. Mater. 25 (2013) 4573–4579, https://doi.org/10.1002/adma.201301579.
- [33] R. Lazzari, N. Vast, J.M. Besson, S. Baroni, A. Dal Corso, Atomic structure and vibrational properties of icosahedral B₄C boron carbide, Phys. Rev. Lett. 83 (1999) 3230–3233.
- [34] Y. Gu, L. Chen, Y. Qian, W. Zhang, J. Ma, Synthesis of nanocrystalline boron carbide via a solvothermal reduction of CCl₄ in the presence of amorphous boron powder, J.

- Am. Ceram. Soc. 88 (2005) 225–227, https://doi.org/10.1111/j.1551-2916.2004. 00023.x.
- [35] X.Y. Tao, Z. Fan, B.J. Nelson, G. Dharuman, W. Zhang, L. Dong, X.D. Li, Internal electron tunneling enabled ultrasensitive position/force peapod sensors, Nano Lett. 15 (2015) 7281–7287, https://doi.org/10.1021/acs.nanolett.5b02362.
- [36] S. Song, W. Xu, R. Cao, L. Luo, M.H. Engelhard, M.E. Bowden, B. Liu, L. Estevez, C.M. Wang, J.G. Zhang, B₄C as a stable non-carbon-based oxygen electrode material for lithium-oxygen batteries, Nano Energy 33 (2017) 195–204, https://doi.org/10.1016/j.nanoen.2017.01.042.
- [37] W.T. Grubb, D.W. Mckee, Boron carbide, a new substrate for fuel cell electrocatalysts, Nature 210 (1966) 192–194.
- [38] A.A. Kuzubov, A.S. Fedorov, N.S. Eliseeva, F.N. Tomilin, P.V. Avramov, D.G. Fedorov, High-capacity electrode material BC₃ for lithium batteries proposed by ab initio simulations, Phys. Rev. B. 85 (2012) 195415, https://doi.org/10.1103/ PhysRevB.85.195415.
- [39] M. Minakshi, M.G. Blackford, G.J. Thorogood, T.B. Issa, The effect of B_4C addition to MnO_2 in a cathode material for battery applications, Electrochim. Acta 55 (2010) 1028-1033, https://doi.org/10.1016/j.electacta.2009.09.062.
- [40] X. Chen, X. Li, F. Ding, W. Xu, J. Xiao, Y. Cao, P. Meduri, J. Liu, G.L. Graff, J.G. Zhang, Conductive rigid skeleton supported silicon as high-performance Li-Ion battery anodes, Nano Lett. 12 (2012) 4124–4130, https://doi.org/10.1021/ nl301657y.
- [41] L. Luo, S.H. Chung, H. Yaghoobnejad Asl, A. Manthiram, Long-life lithium-sulfur batteries with a bifunctional cathode substrate configured with boron carbide nanowires. Adv. Mater. 30 (2018). https://doi.org/10.1002/adma.201804149.
- [42] R.S. Wagner, W.C. Ellis, Vapor-liquid-solid mechanism of single crystal growth, Appl. Phys. Lett. 4 (1964) 89–90, https://doi.org/10.1063/1.1753975.
- [43] X.Y. Tao, L. Dong, X. Wang, W. Zhang, B.J. Nelson, X.D. Li, B₄C-nanowires/carbon-microfiber hybrid structures and composites from cotton T-shirts, Adv. Mater. 22 (2010) 2055–2059, https://doi.org/10.1002/adma.200903071.
- [44] N.N. Song, X.D. Li, Unveiling polytype transformation assisted growth mechanism in boron carbide nanowires, J. Cryst. Growth 481 (2018) 11–17, https://doi.org/10.1016/j.jcrysgro.2017.10.013.
- $[45]\ W.S.\ Hummers, R.E.\ Offeman,\ Preparation\ of\ graphitic\ oxide,\ J.\ Am.\ Chem.\ Soc.\ 80\\ (1958)\ 1339,\ https://doi.org/10.1021/ja01539a017.$
- [46] S. Plimpton, Fast parallel algorithms for short-range molecular dynamics, J. Comput. Phys. 117 (1995) 1–19, https://doi.org/10.1006/jcph.1995.1039.
- [47] S.J. Clark, M.D. Segall, C.J. Pickard, P.J. Hasnip, M.I.J. Probert, K. Refson, M.C. Payne, First principles methods using CASTEP, Z. Krist. 220 (2005) 567–570, https://doi.org/10.1524/zkri.220.5.567.65075.
- [48] N. Dugan, Ş. Ērkoç, Structural properties of boron carbide nanoparticles: application of a new set of Stillinger–Weber parameters, Comput. Mater. Sci. 50 (2011) 2950–2954, https://doi.org/10.1016/j.commatsci.2011.05.012.
- [49] S.J. Stuart, A.B. Tutein, J.A. Harrison, A reactive potential for hydrocarbons with intermolecular interactions, J. Chem. Phys. 112 (2000) 6472–6486, https://doi. org/10.1063/1.481208.
- [50] A.C.T. Van Duin, S. Dasgupta, F. Lorant, W.A. Goddard, ReaxFF: a reactive force field for hydrocarbons, J. Phys. Chem. A. 105 (2001) 9396–9409, https://doi.org/ 10.1021/jp004368u.
- [51] M.M. Islam, A. Ostadhossein, O. Borodin, A.T. Yeates, W.W. Tipton, R.G. Hennig, N. Kumar, A.C.T. van Duin, ReaxFF molecular dynamics simulations on lithiated sulfur cathode materials, Phys. Chem. Chem. Phys. 17 (2015) 3383–3393, https://doi.org/10.1039/C4CP04532G.
- [52] A.D. MacKerell, D. Bashford, M. Bellott, R.L. Dunbrack, J.D. Evanseck, M.J. Field, S. Fischer, J. Gao, H. Guo, S. Ha, D. Joseph-McCarthy, L. Kuchnir, K. Kuczera, F.T.K. Lau, C. Mattos, S. Michnick, T. Ngo, D.T. Nguyen, B. Prodhom, W.E. Reiher, B. Roux, M. Schlenkrich, J.C. Smith, R. Stote, J. Straub, M. Watanabe, J. Wiórkiewicz-Kuczera, D. Yin, M. Karplus, All-atom empirical potential for molecular modeling and dynamics studies of proteins, J. Phys. Chem. B. 102 (1998) 3586–3616, https://doi.org/10.1021/jp973084f.
- [53] C.H. Yu, S. Cukierman, R. Pomès, Theoretical study of the structure and dynamic fluctuations of dioxolane-linked gramicidin channels, Biophys. J. 84 (2003) 816–831, https://doi.org/10.1016/S0006-3495(03)74901-7.
- [54] G. Cinacchi, F. Ingrosso, A. Tani, Solvation dynamics by computer simulation: coumarin C153 in 1,4-dioxane, J. Phys. Chem. B. 110 (2006) 13633–13641, https://doi.org/10.1021/jp0616765.
- [55] G.D. Smith, R.L. Jaffe, D.Y. Yoon, A force field for simulations of 1,2-dimethox-yethane and poly(oxyethylene) based upon ab Initio electronic structure calculations on model molecules, J. Phys. Chem. 97 (1993) 12752–12759, https://doi.org/10.1021/j100151a021.
- [56] N. Hong, M.A. Langell, J. Liu, O. Kizilkaya, S. Adenwalla, Ni doping of semiconducting boron carbide, J. Appl. Phys. 107 (2010), https://doi.org/10.1063/1. 3284205
- [57] M.K. Kolel-Veetil, R.M. Gamache, N. Bernstein, R. Goswami, S.B. Qadri, K.P. Fears, J.B. Miller, E.R. Glaser, T.M. Keller, Substitution of silicon within the rhombohedral boron carbide (B₄C) crystal lattice through high-energy ball-milling, J. Mater. Chem. C. 3 (2015) 11705–11716, https://doi.org/10.1039/c5tc02956b.
- [58] C. Zu, A. Manthiram, Hydroxylated graphene-sulfur nanocomposites for high-rate lithium-sulfur batteries, Adv. Energy Mater. 3 (2013) 1008–1012, https://doi.org/ 10.1002/aenm.201201080.
- [59] L. Ji, M. Rao, H. Zheng, L. Zhang, Y. Li, W. Duan, J. Guo, E.J. Cairns, Y. Zhang, Graphene oxide as a sulfur immobilizer in high performance lithium/sulfur cells, J. Am. Chem. Soc. 133 (2011) 18522–18525, https://doi.org/10.1021/ja206955k.
- [60] D.R. Tallant, T.L. Aselage, A.N. Campbell, D. Emin, Boron carbide structure by Raman spectroscopy, Phys. Rev. B. 40 (1989) 5649–5656, https://doi.org/10. 1103/PhysRevB.40.5649.

- [61] Z. Wang, Y. Dong, H. Li, Z. Zhao, H. Bin Wu, C. Hao, S. Liu, J. Qiu, X.W.D. Lou, Enhancing lithium-sulphur battery performance by strongly binding the discharge products on amino-functionalized reduced graphene oxide, Nat. Commun. 5 (2014) 1–8, https://doi.org/10.1038/ncomms6002.
- [62] J. Shim, K.A. Striebel, E.J. Cairns, The lithium/sulfur rechargeable cell, J. Electrochem. Soc. 149 (2002) A1321, https://doi.org/10.1149/1.1503076.
- [63] R. Elazari, G. Salitra, A. Garsuch, A. Panchenko, D. Aurbach, Sulfur-impregnated activated carbon fiber cloth as a binder-free cathode for rechargeable Li-S batteries, Adv. Mater. 23 (2011) 5641–5644, https://doi.org/10.1002/adma.201103274.
- [64] Y.C. Lu, Q. He, H.A. Gasteiger, Probing the lithium-sulfur redox reactions: a rotating-ring disk electrode study, J. Phys. Chem. C. 118 (2014) 5733–5741, https://doi.org/10.1021/jp500382s.
- [65] F.Y. Fan, W.C. Carter, Y.-M. Chiang, Mechanism and kinetics of Li₂S precipitation in lithium-sulfur batteries, Adv. Mater. 27 (2015) 5203–5209, https://doi.org/10. 1002/adma.201501559.
- [66] W.C. Oliver, G.M. Pharr, An improved technique for determining hardness and elastic modulus using load and displacement sensing indentation experiments, J. Mater. Res. 7 (1992) 1564–1583, https://doi.org/10.1557/JMR.1992.1564.